



TECHNICAL ARTICLE

Numerical Modeling of Selective Laser Melting: Influence of Process Parameters on the Melt Pool Geometry

Anuj Kumar and Mukul Shukla

Submitted: 9 July 2022 / Revised: 20 October 2022 / Accepted: 19 November 2022 / Published online: 1 December 2022

An efficient approach for virtual prediction of melt pool geometry and temperature distribution in selective laser melting (SLM) is required to optimize the process parameters for eventually printing high-fidelity parts. In this study, the melt pool geometry in the SLM process was simulated by employing Ansys Additive, the commercial finite element analysis software tool. First, a single track of 4 mm length was modeled for Inconel 718 material by varying the process parameters. Validations with existing studies were performed to ensure the reliability of the FE model. Further, a process map exhibiting the optimum process parameters window for SLMed Inconel 718 was developed, which can be used to avoid process-induced defects such as lack of fusion, balling, and keyholing. The response surface methodology design of experiment technique and ANOVA-based regression modeling were used to relate the vital SLM process parameters with the melt pool geometry. The statistical analysis results showed that maximum melt pool depth and width are obtained at maximum laser power and at minimum scan speed and layer thickness. The proposed approach facilitates robust 3D printing by avoiding common process-induced defects as well as allows the tuning of vital process parameters for fabricating superior quality SLM builds.

Keywords finite element simulation, Inconel 718, melt pool geometry, process map, response surface methodology, selective laser melting

1. Introduction

In the recent past, metal additive manufacturing (MAM) has emerged as one of the most promising advanced manufacturing processes for fabricating complex functional components that would otherwise be impossible using traditional manufacturing processes (Ref 1). It negates the need for expensive tooling. MAM is used to fabricate parts by melting metal powders, wires, or sheets. Binder jetting, directed energy deposition, and powder bed fusion (PBF) are among the popular subcategories of MAM (Ref 2). These processes are widely used to produce geometrically complex products with high geometric precision, desired grain structure, and superior mechanical properties. They have a broad range of applications in the aerospace, automobile, and medical sectors (Ref 3). Selective laser melting (SLM) is a prominent PBF technology that involves dispersing metallic powder on a substrate and fusing it together in layered manner with a moving laser that selectively melts the powder particles. A typical configuration of the SLM process is shown (see Fig. 1). The melt pool characteristic is

commonly employed as a process monitoring signature in SLM processes as it is directly correlated with the development of porosity and other build defects (Ref 4). Laser power, scan speed, layer thickness, and laser spot diameter are just a few of the numerous process parameters that influence the melt pool characteristics and hence the build quality of the part (Ref 5). In the SLM process, the laser power and scan speed are the commonly varied process parameters to control the melt pool geometry and the quality of build (Ref 6). A potential remedy for reducing process-induced defects is to predict and control the melt pool geometry during the build process. Apart from being a useful tool to assess and minimize defects, melt pool geometry is also utilized in process-parameter optimization, residual stress and distortion estimation, grain growth evolution, and process–structure–property linkage (Ref 7). To achieve these objectives, an accurate prediction of the melt pool geometry with a given combination of process parameters is very much desired. The next section reviews the literature to identify the gaps in the melt pool geometry studies, followed by the implemented numerical approach, results, and conclusions of this study.

2. Literature Review

The melt pool geometry is a distinctive index that reflects the quality of the SLM process. A melt pool that is too deep is more prone to keyhole formation, which increases porosity in the build (Ref 8). Furthermore, if the melt pool is too shallow to completely melt the powder layer, lack of fusion porosity may occur. In the multi-track SLM process, irregular pores can also be formed by an insufficient overlap of neighboring tracks, which is influenced by melt pool geometry and hatch spacing between neighboring tracks (Ref 9). These pores may have an

Anuj Kumar, Department of Mechanical Engineering, Motilal Nehru National Institute of Technology Allahabad, Prayagraj 211004, India; and **Mukul Shukla**, Department of Mechanical Engineering, Motilal Nehru National Institute of Technology Allahabad, Prayagraj 211004, India; and Department of Mechanical and Industrial Engineering Technology, University of Johannesburg, Johannesburg, South Africa. Contact e-mails: mukulshukla@mnnit.ac.in and mukuls@uj.ac.za.

adverse effect on the mechanical performance of the build. SLM builds are also prone to balling defects when a solidified molten pool fails to adequately wet a solid part below (Ref 10). This results in the formation of discontinuous tracks, which

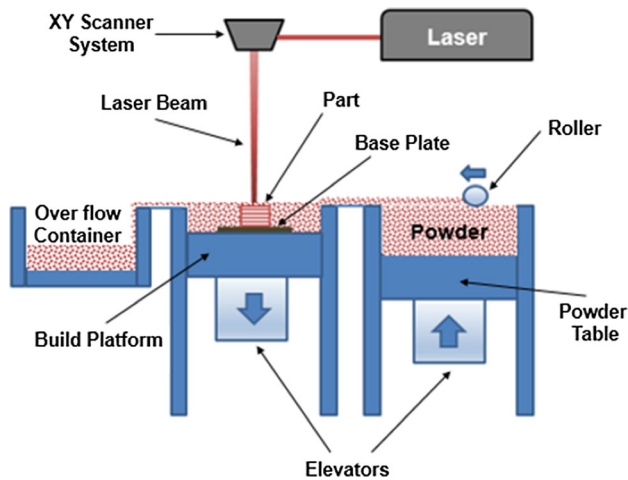


Fig. 1 A typical SLM process configuration

deteriorates the build's surface quality. Figure 2 shows optical microscopy images of the process-induced defects in the SLMed build that were formed by the lack of fusion, balling, shrinkage, and keyholing (Ref 11).

The melt pool geometry is also shown to have a significant influence on the dimensional accuracy of the SLMed builds. Thus, controlling the geometry of the melt pool helps to eliminate numerous potential defects and optimize the final quality of the builds (Ref 12). The literature exhibits that the evaluation of melt pool geometry along with thermal history is important as these two are crucial in determining the resulting grain structure and mechanical properties (Ref 13, 14). As the melt pool geometry and temperature distribution are of great importance, researchers utilized various sensors for monitoring and controlling the SLM process (Ref 15). Incorporating monitoring sensors, calibrating them, and analyzing the acquired data are expensive in terms of both time and capital (Ref 16).

Single-track build experiments have been used to investigate the relationships between processing parameters and melt pool geometry, which proved to be cost and time efficient. They make it convenient to evaluate the individual effects of a specific processing parameter on the melt pool geometry. Developing a generic criterion for predicting melt pool

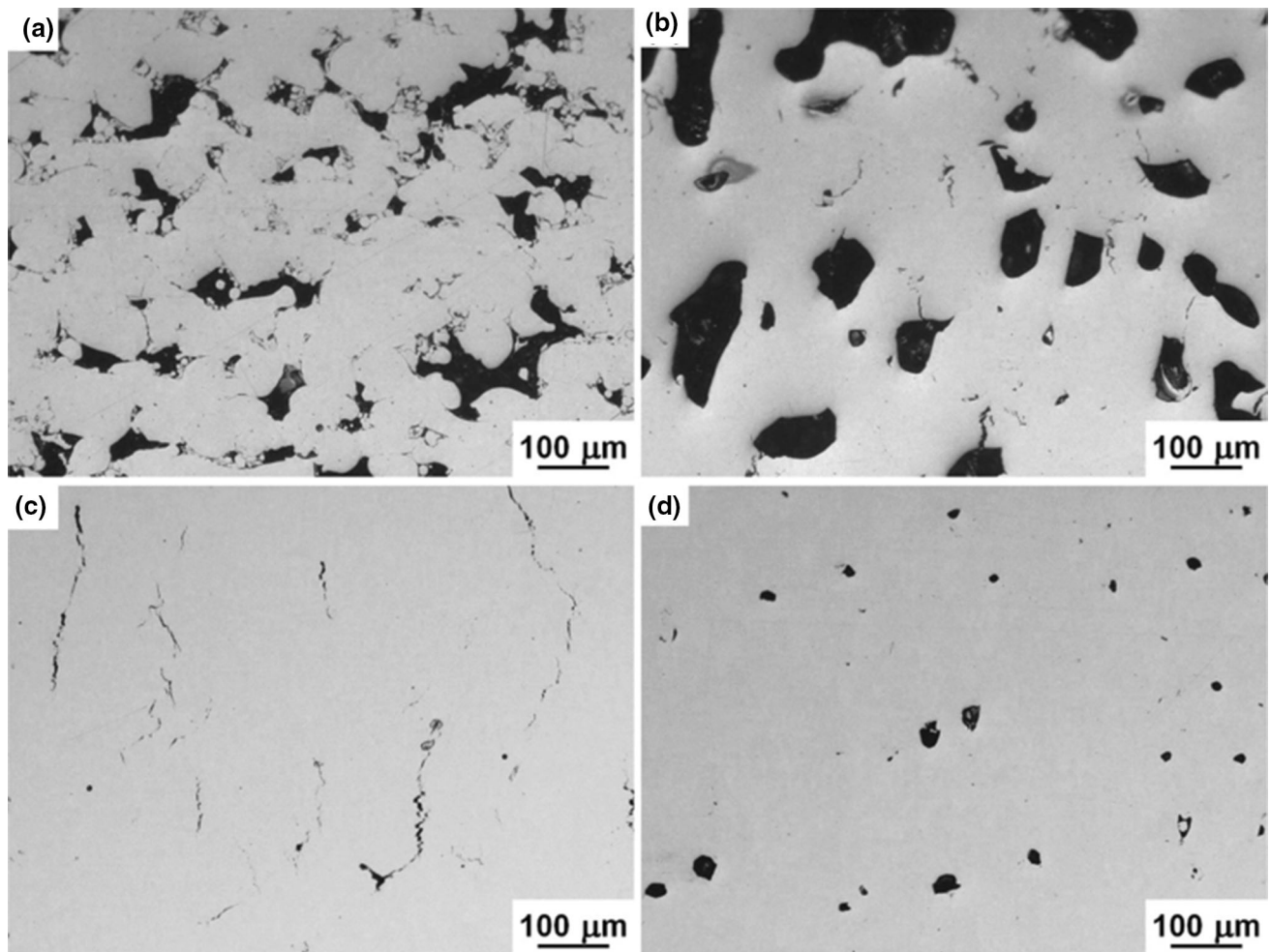


Fig. 2 Process-induced defects in SLM (a) lack of fusion (b) balling (c) shrinkage (d) keyholing (Ref 11). Figure 4 by Won Rae Kim, Gyung Bae Bang, Jung Hyun Park et al. in *Journal of Materials Research and Technology*, Vol 9, Iss 6, Pages 12,834–12,839 is licensed under CC BY-NC-ND 4.0

geometry is challenging since the SLM process comprises numerous process parameters that affect melt pool characteristics (Ref 17). Along with experimental approaches, numerical simulations have also been utilized to study the melt pool characteristics and thermal history in the SLM process (Ref 18).

Most numerical simulations in the literature are developed based on the physics involved in the SLM process, such as rapid heat transfer, surface tension, molten metal flow, and recoil pressure. These numerical modeling approaches prove to be reliable for simulating the melt pool geometry and temperature distribution in SLM process as they also explicitly unravel the underlying physics. Cheng et al. (Ref 19) developed a multiphysics computational fluid dynamics model to predict the melt pool geometry and pore defects during laser melting of a SS-316L. Khorasani et al. (Ref 20) developed a micro-scale thermo-fluid model in a commercial software Flow 3d to investigate melt pool depth with varying process conditions. However, the multiscale and multiphysics nature of the numerical problem imposes a very high computational cost, preventing their widespread acceptance (Ref 21, 22).

In parallel, there are several studies of melt pool evolution in which the developed thermal models are based primarily on solving the heat conduction equations using finite element methods (Ref 23, 24). Tan et al. (Ref 25) studied the melt pool evolution in SLM by solving the transient heat conduction equation, but the effect of vital process parameters on melt pool geometry was not evaluated. Arisoy et al. (Ref 26) evaluated melt pool geometry during selective laser build at three distinct locations, the start, middle, and end of the track using thermal imaging and numerical methods. Though the simulation results are satisfactory, the approach was computationally expensive. Ansari et al. (Ref 27) developed a finite element model to evaluate the influence of process parameters on the melt pool and peak temperature. Because fewer combinations of laser power and scan speed were used, the impact on process-induced defects could not exactly be determined. Waqar et al. (Ref 28) performed multi-track and multi-layer numerical modeling to investigate the thermal behavior and melt pool characteristics. Majeed et al. (Ref 29) developed a three-dimensional finite element model to analyze the influence of laser processing parameters on different underlying surfaces.

Recently, data-driven techniques are gaining a lot of popularity in every domain of research, including AM (Ref 30, 31). The high dimensionality and complexity of the SLM process make it well-suited for applying the popular machine learning (ML) algorithms, and the synergy of ML and simulation can accelerate computations by orders of magnitude above standalone physics-based simulations (Ref 32). Moreover, as the SLM process modeling yields a huge amount of data in terms of process parameters, simulated melt pool geometry, and temperature distribution profiles, ML algorithms can be applied to these data in order to learn hidden relationships and correlations among the vital entities. However, one of the major challenges of leveraging ML techniques in AM is the availability of smaller-size datasets, particularly for a variety of input process conditions. (Ref 33).

It is concluded from the literature review that a comprehensive study of the melt pool geometry is essential for the deployment of the SLM process for real-life industrial applications. The majority of the reviewed literature focused on evaluating the melt pool geometry either using laborious and expensive experimental studies or computationally expensive numerical simulations, limiting these approaches for detailed

exploration of the SLM process. The above methods also act as a bottleneck for the application of emerging data-driven techniques, as the acquired data are either expensive and/or very limited. Moreover, the development of process maps representing optimum process windows to avoid process-induced defects such as lack of fusion, keyholing and balling has not been well-established utilizing numerical simulations. The development of effective virtual simulation tools and computing techniques has significantly contributed to the emergence of increasingly efficient, quick and powerful frameworks to assess the fidelity of printed parts.

This study addressed the above-mentioned issues by employing a robust FE modeling approach for rapid prediction of melt pool geometry using a commercial simulation tool. The proposed method not only allows for the simulation of melt pool characteristics in SLM, but also for the eventual development of process maps for defect-free builds. Correlation between the melt pool geometry and the SLM input parameters (laser power, scan speed, and powder layer thickness) was developed using a response surface methodology-based statistical analysis, and different quadratic response models were developed. SLM parameters were also optimized using RSM for suitable melt pool depth and width for a defect-free build with improved microstructure and mechanical properties. This work is aimed at supporting the decision-making process toward high fidelity AM, with minimum number of trial runs and thereby cost.

3. Material and Methods

The numerical approach incorporated in this study is shown (see Fig. 3). The first part of the approach, single bead simulation, was employed to model the melt pool geometry of single-track SLMed Inconel 718. It facilitated the detection of process-induced defects (lack of fusion, balling, and keyholing) and the generation of process maps. The second part of the approach, which is currently a work in progress, uses the optimized process parameters from these process maps for thermal history and microstructure simulation in multi-track and multi-layer SLM.

3.1 Governing Equations and Boundary Conditions

The SLM process is governed by numerous input process parameters like laser power (P), scan speed (v), powder layer thickness (t) and hatch distance (h) to name a few important ones. The laser energy density (E) of the process in terms of these key process parameters can be determined using formulae below (Ref 34):

$$E = \frac{P}{v \cdot t \cdot h} \text{ (J/mm}^3\text{)} \quad \text{(Eq 1)}$$

If the process parameters are not properly tuned, improper melting can result in a variety of undesirable process-induced defects or even a complete build failure.

The temperature distribution $T(x, y, z, t)$ is determined in the ANSYS Additive module by solving the governing three-dimensional partial differential equation of transient heat transfer, which is defined as (Ref 35):

$$\rho c \frac{\partial T}{\partial t} = \frac{\partial}{\partial x} \left(k \frac{\partial T}{\partial x} \right) + \frac{\partial}{\partial y} \left(k \frac{\partial T}{\partial y} \right) + \frac{\partial}{\partial z} \left(k \frac{\partial T}{\partial z} \right) + q \quad \text{(Eq 2)}$$

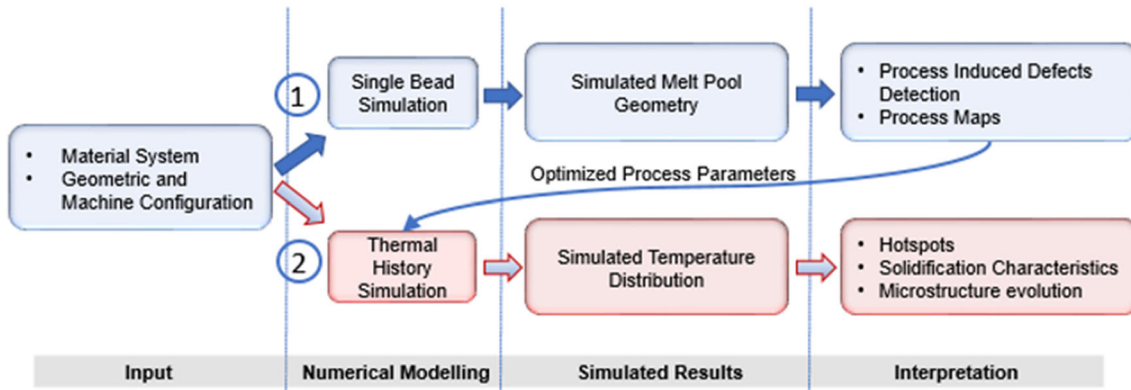


Fig. 3 Workflow of the proposed numerical approach: (1) single bead simulation conducted in this study and (2) thermal history simulation (currently in progress)

In the above equation, T the temperature varies as a function of time and location, while ρ , c and k are the material density, specific heat, and thermal conductivity, respectively. Further, t is the interaction time, and q is the heat generated per volume within the build.

At time $t = 0$, the initial condition of powder bed regarding thermal distribution can be defined as follows:

$$T(x, y, z, t)_{t=0} = T_0(x, y, z) \in D \quad (\text{Eq 3})$$

where T_0 is the ambient temperature, and D is the concerned domain. The natural boundary condition with heat balance can be represented as:

$$k \frac{\partial T}{\partial n} + q_r + q_c = q(x, y, z) \in S \quad (\text{Eq 4})$$

where S is the surfaces of levied heat fluxes, convection and radiation and n is the normal vector to the surface S .

Heat flux input q due to the laser beam source is considered to have a Gaussian distribution and is defined by (Ref 36):

$$q = \frac{2AP}{\pi R^2} \exp\left(-\frac{2r^2}{R^2}\right) \quad (\text{Eq 5})$$

where A is the laser absorptance of powder material, P is the laser power, R is the effective radius of laser beam, and r represents the radial distance from the center of the laser spot to a point on the powder bed surface. Further, q_c represents the heat transfer due to convection and can be defined by:

$$q_c = h(T - T_0) \quad (\text{Eq 6})$$

while q_r represents the heat transfer due to radiation and can be expressed by:

$$q_r = \sigma \varepsilon (T^4 - T_0^4) \quad (\text{Eq 7})$$

where h , σ , and ε represent the convective heat transfer coefficient, the Stefan–Boltzmann constant, and the surface emissivity, respectively.

3.2 Finite Element Modeling

In this study, several physical assumptions were considered for modeling the SLM process. The powder bed was assumed to be a continuous and homogeneous media. The thermo-physical properties, such as thermal conductivity and specific

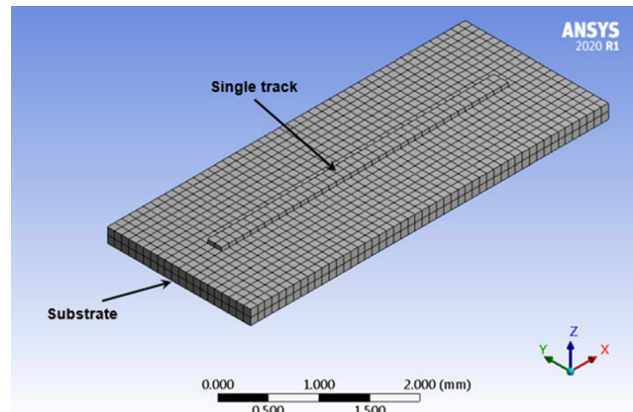


Fig. 4 Meshed model used for FE simulation

heat capacity of the material, were considered to be temperature dependent. The convective heat transfer coefficient between the powder bed and the surroundings was treated as constant.

ANSYS Multiphysics (2020R1) with Additive Wizard was used in this study for numerical modeling. The finite element model with meshing of single bead and substrate is depicted in Fig. 4. The base plate with the dimensions of $5 \times 2 \times 0.2 \text{ mm}^3$ was taken as substrate, and the laser scan area on the IN718 powder bed had a length of 4 mm. Considering the computational efficiency (MRF), hexahedral meshing with a fine mesh of 0.1 mm was used and the number of elements was 2168.

A voxel is a hexahedral (cubic) element used in the FE analysis to specify the domain. The computational domain is divided into voxels using the voxelization function, and to more accurately depict the domain, sub-voxels are used within each voxel. The voxel size ranges from 0.2 to 2 mm. While the mesh in the mechanics solver is determined by the voxel size and voxel sample rate, the Additive application uses mesh resolution factor (MRF) to control the mesh in the thermal Solver. MRF controls the fidelity of the solution by scaling the mesh for the thermal solver.

Valid MRF values are integers between 1 and 12. The MRF of 12 corresponds to a voxel rate of 1, resulting in a coarse mesh, and as the MRF is reduced, the mesh becomes finer. MRF values with different voxel rate are represented in Fig. 5. MRF is inversely proportional to the run time and fidelity. If the

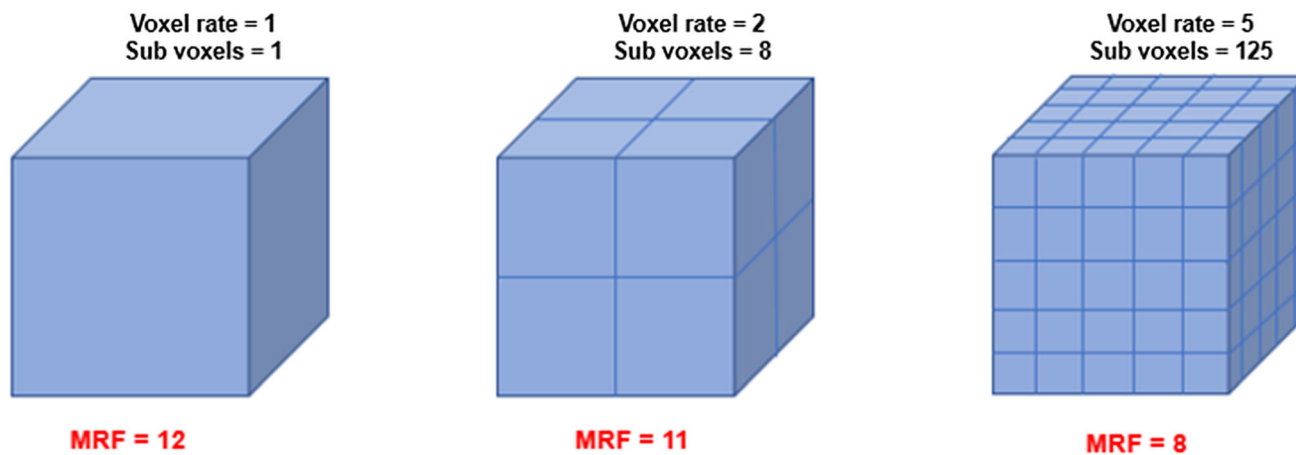


Fig. 5 Mesh resolution factor (MRF) with different voxel rates

Table 1 Material properties for IN718 used in the numerical simulation (Ref 37)

Properties	Values
Liquidus temperature, K	1609
Solidus temperature, K	1533
Thermal conductivity, W/m K	$0.56 + 2.9 \times 10^{-2} T - 7 \times 10^{-6} T^2$
Specific heat capacity, J/kg K	$360.4 + 0.026 T - 4 \times 10^{-6} T^2$
Density, kg/m ³	8100
Latent heat of fusion, J/kg	209×10^3
Viscosity, kg/m s	5×10^{-3}
Laser absorptance, A	0.7

MRF is too low, the simulation will take a long time to complete due to the finer mesh used in the thermal solution. If the MRF is too high, the simulation time will be less but accuracy is lost as the mesh used is too coarse to accurately resolve the melt pool. This indicates that the element size is too large to adequately represent the heat transfer in the melt pool. A trade-off between simulation time and model accuracy allowed us to take an informed decision of the final MRF. Tuning the MRF by comparing simulated melt pool geometry with existing experimental results leads to selection of final MRF as 4.

3.3 Material Properties and Simulation Parameters

The material data for Inconel 718 used in this study were obtained from ANSYS Mechanical engineering data source, additive manufacturing materials. The thermo-physical properties and their values used in the numerical models are documented in Table 1.

4. Single Bead Parametric Simulation

At first, a single track was simulated to determine the melt pool characteristics for a given process parameters and material system. It replicated the standard practice of printing a single track on SLM systems where the heat source scans in a single stroke across the powder bed. The simulated melt pool depth and width were evaluated to assess the effect of SLM process

parameters on the melt pool geometry without experimenting on expensive machine and material systems. The input process parameters with the machine configuration are used to simulate a definite track length in geometric configuration. The layer thickness, laser spot size, and baseplate temperature were used as constant inputs, whereas the laser power and scan speed were employed as parametric variables. A schematic of the numerical model representing the single bead parametric simulation and the melt pool geometry is shown (see Fig. 6).

Single tracks of 4 mm length SLMed Inconel 718 were simulated to evaluate the geometry of melt pool. Considering the laser power and scan speed range used by various researchers (Ref 38-41) for Inconel 718, nine combinations of the laser power and scan speed were selected. Combinations of laser power, scan speed, and energy density used in the single bead simulation are shown in Table 2. Other constant input parameters included layer thickness of 30 μm , laser spot size of 80-100 μm , and the base plate temperature of 80 $^{\circ}\text{C}$.

The melt pool geometry for these nine combinations was evaluated from single bead simulation, and the effect of laser power and scan speed on melt pool depth and width is shown in Fig. 7(a) and (b), respectively.

The effect of laser energy density on melt pool depth and width was also studied (see Fig. 8). As the laser energy density increases, melt pool depth and width increase as more energy is transferred to the melt pool area. This single bead simulation of melt pool geometry took 110 min of computational time on a workstation equipped with an Intel octa-core i3 3.1 GHz CPU and 8 GB of RAM. So, this proposed framework can be utilized for rapid evaluation of melt pool geometry with a given material system and process conditions in SLM. This rapid prediction of melt pool geometry was efficiently utilized in developing the process map for the SLM process to avoid common defects in the build. This was comprehensively discussed later in the study.

4.1 Model Validation

Prior to incorporating the numerical model for developing process maps, it was validated by comparing the simulated results of melt pool geometry with the existing literature. Bayat et al. (Ref 42) evaluated single-track melt pool geometry for SLMed Inconel 718. The track length for the study was 1000 μm , and a layer of powder with a thickness of 40 μm was

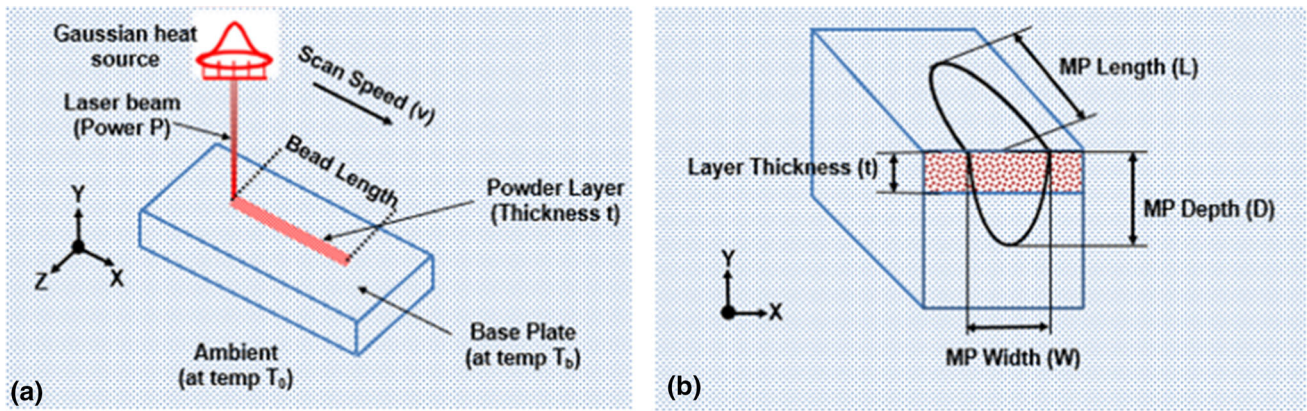
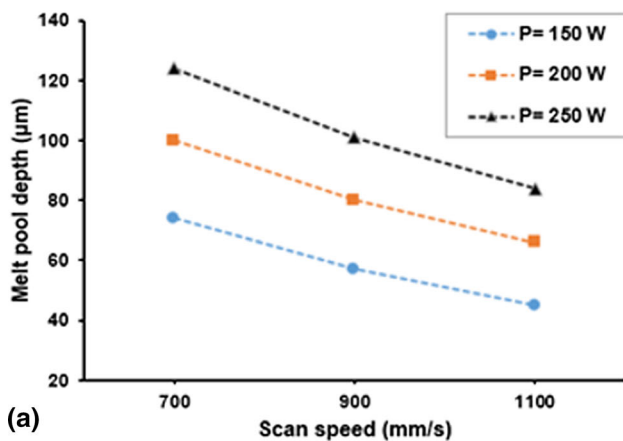


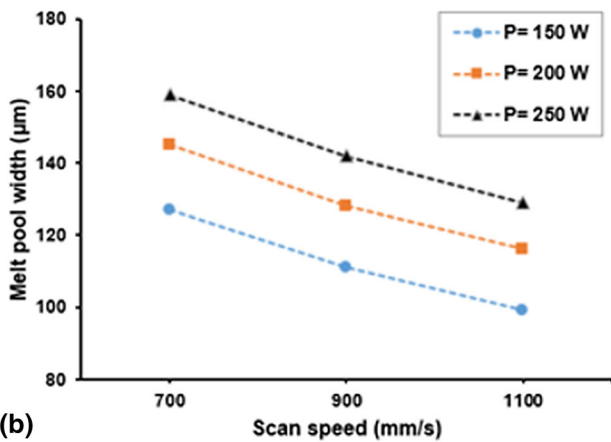
Fig. 6 Schematic showing the physical model: (a) single bead parametric simulation depicting Gaussian heat source and (b) simulated melt pool geometry

Table 2 Various combinations used in the single bead simulation

Laser power, W	150	200	250	150	200	250	150	200	250
Scan speed, mm/s	700	700	700	900	900	900	1100	1100	1100
Energy density, J/mm	0.214	0.286	0.357	0.167	0.222	0.278	0.136	0.182	0.227



(a)



(b)

Fig. 7 Variation of (a) melt pool depth and (b) melt pool width with laser power and scan speed

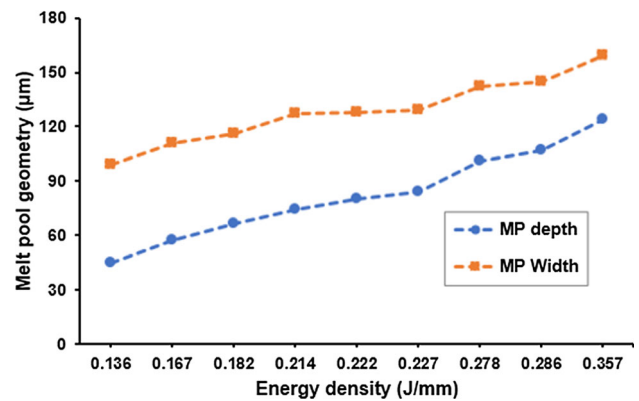


Fig. 8 Variation of melt pool depth and width with energy density

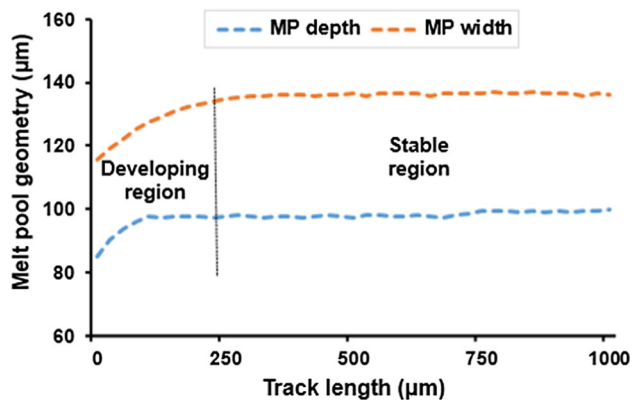
laid using the process conditions given in Table 3. Melt pool depth and width were determined along the track, with values ranging from 90-99 for melt pool depth and 120-136 μm for melt pool width.

To validate the model, the above-mentioned single track of 1000 μm was simulated with the same process conditions and material systems. The melt pool depth and width simulated over the track length are shown in Fig. 9. At the start of the track, the melt pool depth and width were increasing as the melt pool was in the developing region. To analyze the simulated results, melt pool geometry was taken from the stable region where the melt pool was already developed. The simulated melt pool depth and width were compared with actual results and are listed in Table 4. The simulated melt pool geometry was clearly in good accord with the results obtained by Bayat et al. (Ref 42).

Kusuma et al. (Ref 43) printed single tracks with varying laser power and scan speed by laying 50 μm powder layers and using a laser source of 100 μm spot size. Experimentally measured melt pool widths for various combinations used in the

Table 3 Process conditions for the validation study

Laser power, W	Scan speed, mm/s	Layer thickness, μm	Base plate temperature, $^{\circ}\text{C}$	Laser spot size, μm
285	960	40	50	100

**Fig. 9** Melt pool depth and width over the simulated track length

study are shown in Table 5. To further assess the robustness of the approach, single bead simulation is employed to model single track with same process parameters as utilized by experimental study. 10 single tracks were simulated, and their melt pool widths were compared with the experimental widths as listed in Table 5. The simulation results give a good agreement with the experimental findings.

Jakumeit et al. (Ref 44) printed five single tracks with different laser energy densities by laying 60 μm powder layers and using a laser heat source of 100 μm spot size. Experimentally measured melt pool depth for various combinations of laser power and scan speed used in the study is shown in Table 6. Five single tracks with these process parameters were simulated using single bead simulation, and their melt pool depths were compared with the experimental depths and are

Table 4 Actual (Ref 42) and simulated melt pool geometry

MP geometry	Actual MP depth, μm	Simulated MP depth, μm	Actual MP width, μm	Simulated MP width, μm
Values	90-99	94	120-136	127

Table 5 Experimental (Ref 43) and simulated MP widths

Laser power, W	Scan speeds, mm/s					
	500			600		
	Experimental MP width, μm	Simulated MP width, μm	Absolute error, %	Experimental MP width, μm	Simulated MP width, μm	Absolute error, %
100	163	160	1.84	150	147	2.00
120	168	178	5.95	164	167	1.83
140	194	192	1.03	170	176	3.53
160	210	201	4.29	190	187	1.58
180	217	209	3.69	200	195	2.50

Table 6 Experimental (Ref 44) and simulated melt pool depths

Laser power, W	Scan speed, mm/s	Energy density, J/mm	Experimental MP depth, μm	Simulated MP depth, μm	Absolute error, %
142	960	0.15	73	76	4.10
250	1100	0.23	120	116	3.33
285	960	0.30	172	157	8.72
250	660	0.38	176	172	2.27
285	600	0.48	252	231	8.33

shown in Fig. 10. The simulation gives a fair agreement with the experimental findings as the calculated absolute errors are < 10%.

4.2 Process Map for SLMed Inconel 718

Process maps provide an optimum process parameter window for a specific material system that can be used to print without encountering major printing defects such as lack of fusion, balling, and keyholing. Single bead simulations were utilized to generate a laser power-scan speed process map for SLMed Inconel 718. Seven different values for laser power and scan speed were used to generate 49 combinations in the laser power-scan speed space. Material system, input process conditions, laser power and scan speed combinations used to develop the process map are given in Table 7 and 8.

The simulated results of melt pool depth (D), width (W), and length (L) are utilized to assess various criteria of defect-free builds in SLMed IN718 (Ref 45). The following constraints on the melt pool geometry were introduced to evaluate the characteristics of the melt pool:

- Ratio of melt pool depth to layer thickness as ($D/t > 2$). It ensures that the melt pool is not too shallow.
- Ratio of melt pool depth to its width as ($D/W < 0.75$). It ensures that the melt pool is not too deep.
- Ratio of melt pool length to its width as ($L/W < 4$). It ensures that the melt pool is not too long.

where t is the powder layer thickness. All these ratios were evaluated for all combinations of laser power and scan speed and plotted in the form of a process map as shown in Fig. 11. The process map exhibited that at low laser power and higher scan speeds, lack of fusion was significant due to energy deficit, which led to improper fusion of powder particles. Keyholing

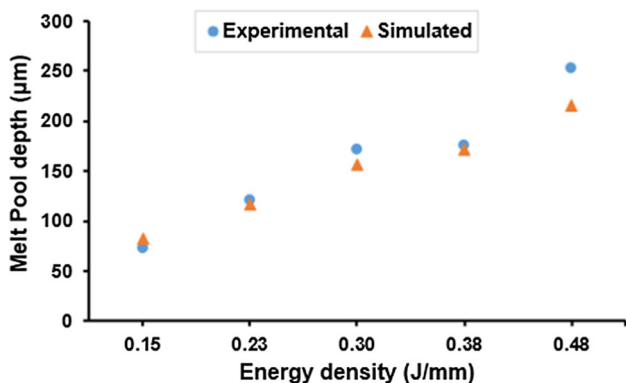


Fig. 10 Simulated vs. experimental (Ref 44) melt pool depths for different energy densities

was observed at higher laser power levels and lower scan speeds due to energy surplus, which resulted in a deeper melt pool.

At higher levels of laser power and scan speed, the width of the melt pool reduced, gradually became discontinuous, and subsequently resulted in balling due to Rayleigh instability. The region free of the aforementioned common flaws was designated as the optimal process window. Of all the process parameter combinations of laser power and scan speed, 10 combinations yielded the optimum process window enclosed by the dotted lines shown in the process map. Within this window, the resulted melt pool geometry is such that the build is likely to be free from lack of fusion, keyholing, and balling. Thus, choosing a laser power and scan speed combination from this optimum process window will be beneficial to further studies of thermal history and microstructure evolution.

An experimental study by Kumar et al. (Ref 46) also supported that the lack of fusion defect is more likely to occur at low laser power and low scan speed combinations. At high laser power and high scan speed combinations, however, balling defects are common. Moreover, the laser power-scan speed combinations used to fabricate nearly defect-free Inconel 718 components are well within the optimized process window developed in this study. Another study by Cheng et al. (Ref 23)

Table 8 Input laser power and scan speed combination used to generate the process map

Laser power, W	50	100	150	200	250	300	350
Scan speed, mm/s	500	600	700	800	900	1000	1100

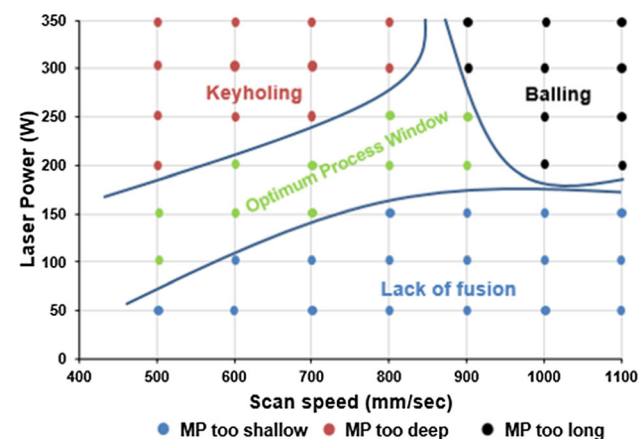


Fig. 11 Process map of laser power vs. scan speed for SLMed Inconel 718

Table 7 Material system and constant input process conditions

Material system	Layer thickness, μm	Laser spot size, μm	Track length, μm	Base plate Temp, $^{\circ}\text{C}$
Inconel 718	30	80-100	4	80

established that a larger laser power and smaller scanning speed are responsible for generating keyhole-induced pores in SLMed builds, as also evident from the developed process map in this study.

5. Design of Experiments

The design of experiment (DOE) was utilized to study the effect of the laser power, scan speed, and layer thickness on the melt pool geometry of the simulated single tracks. DOE is a well-established approach to analyze the influence of input process parameter (factor) on evaluated responses. The analysis of variance (ANOVA) was employed to develop the mathematical relation between the input parameters and the response. Three SLM process parameters were sorted at three uniformly spaced levels, as shown in Table 9. The laser power (P) and scan speed (v) were selected from the developed process map. Then, the range of layer thickness (t) was taken as 30–45 μm to assess the effect on melt pool geometry. Melt pool depth (D) and width (W) were considered as responses for the regression modeling.

Table 9 Levels of selected SLM process parameters for BBD RSM

Parameters	Units	− 1	0	1
Laser power, P	W	150	200	250
Scan speed, v	mm/s	700	800	900
Layer thickness, t	μm	30	45	60

Table 10 BBD RSM process parameter (factors) and responses

Run order	Std. order	Process parameters			Responses	
		Laser power, W	Scan speed, mm/s	Layer thickness, μm	MP depth, μm	MP width, μm
1	6	250	800	30	111	150
2	10	200	900	30	80	128
3	14	200	800	45	78	126
4	7	150	800	60	35	85
5	12	200	900	60	53	100
6	8	250	800	60	92	128
7	15	200	800	45	78	126
8	1	150	700	45	61	116
9	13	200	800	45	78	126
10	3	150	900	45	44	98
11	5	150	800	30	64	118
12	11	200	700	60	77	121
13	2	250	700	45	119	152
14	9	200	700	30	100	145
25	4	250	900	45	92	133

Table 11 Predicted melt pool geometry using regression equations and comparison with simulated results

Run order	Simulated MP depth, μm	Predicted MP depth, μm	Error, %	Simulated MP width, μm	Predicted MP width, μm	Error, %
1	111	113.18	1.96	150	149.29	0.47
2	80	81.60	2.00	128	128.61	0.48
3	78	79.55	1.98	126	126.11	0.08
4	35	35.92	2.63	85	85.92	1.08
5	53	55.08	3.92	100	99.84	0.16
6	92	93.65	1.79	128	128.02	0.01
7	78	79.55	1.98	126	126.11	0.08
8	61	62.43	2.35	116	115.69	0.27
9	78	79.55	1.98	126	126.11	0.08
10	44	45.47	3.34	98	97.42	0.59
11	64	65.44	2.25	118	118.19	0.16
12	77	78.54	2.00	121	120.60	0.33
13	119	119.67	0.56	152	152.79	0.52
14	100	101.06	1.06	145	145.37	0.26
15	92	93.71	1.85	133	133.53	0.40

Table 12 ANOVA table for MP depth and width

Response	Source	Adj SS	F value	P value	T value
MP depth, D R-sq (pred) 99.64%	Linear	7755.75	7286.43	< 0.001	228.36
	<i>P</i>	5565.13	15,900.38	< 0.001	126.10
	<i>v</i>	990.13	2828.93	< 0.001	- 53.19
	<i>t</i>	1200.50	3430.03	< 0.001	- 58.57
MP width, W R-sq (pred) 98.94%	Linear	4798.75	2460.90	< 0.001	270.69
	<i>P</i>	2667.50	4099.23	< 0.001	64.03
	<i>v</i>	703.13	1081.78	< 0.001	- 32.89
	<i>t</i>	1431.13	2201.73	< 0.001	- 46.92

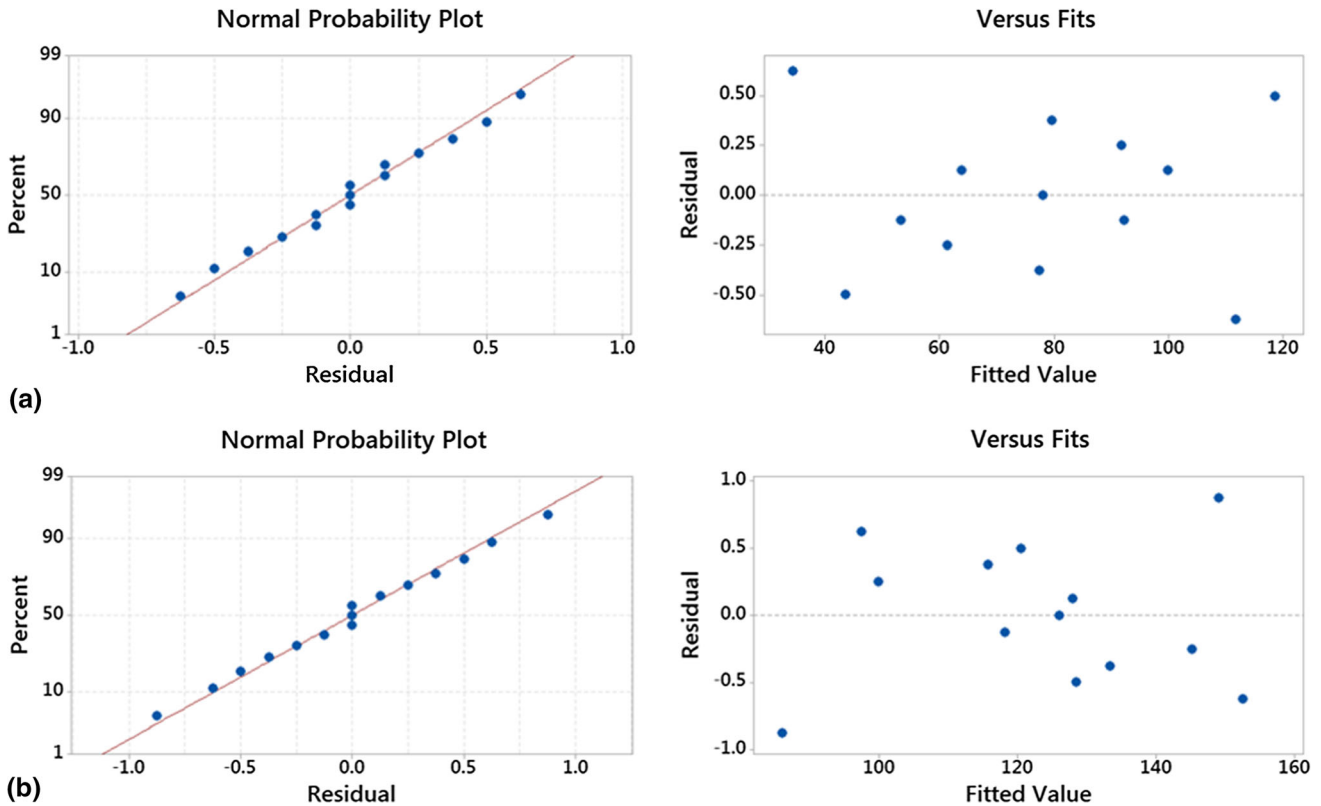


Fig. 12 Normal probability plot and residual vs. fitted value plot for (a) MP depth (b) MP width

5.1 Response Surface Methodology

The response surface methodology (RSM) based on Box–Behnken design (BBD) with a simulation design of 15 runs (with 3 center points) was employed, as shown in Table 10. It facilitates reduced simulation (from 27 of full factorials run to 15 BBD run) and also the development of regression models as BBD allows efficient estimation of the first- and second-order coefficients. 15 single tracks were simulated using single bead simulation by varying laser power, scan speed and layer thickness as per BBD runs while keeping other input parameters fixed to evaluate the responses *D* and *W*. SLM process parameters were also optimized by developing and analyzing regression models using the Minitab statistical software (version 2019). The evaluated responses of the simulated melt pool geometry for the different process parameters are shown in Table 10.

The relationship between the input SLM process parameters and the output responses was evaluated using RSM. The quadratic regression equations for *D* and *W* in terms of the actual parameter values were generated and represented by the below equations:

$$\begin{aligned}
 D = & 93.4 + 0.8375P - 0.2113v - 0.2001t \\
 & - 0.00025P * P + 0.00014v * v - 0.00833t * t \\
 & - 0.00045P * v + 0.00333P * t - 0.000667v * t
 \end{aligned}
 \tag{Eq 8}$$

$$\begin{aligned}
 W = & 165.6 + 0.6010P - 0.2138v + 0.3081t \\
 & - 0.000900P * P + 0.000100v * v - 0.01556t * t \\
 & - 0.000050P * v + 0.003667P * t - 0.000667v * t
 \end{aligned}
 \tag{Eq 9}$$

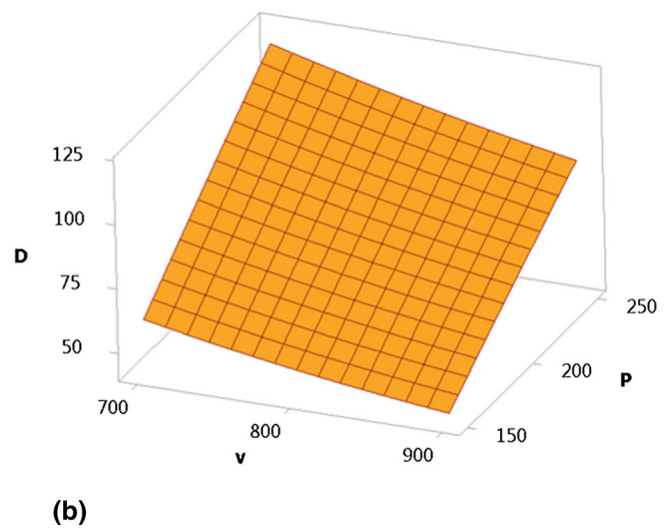
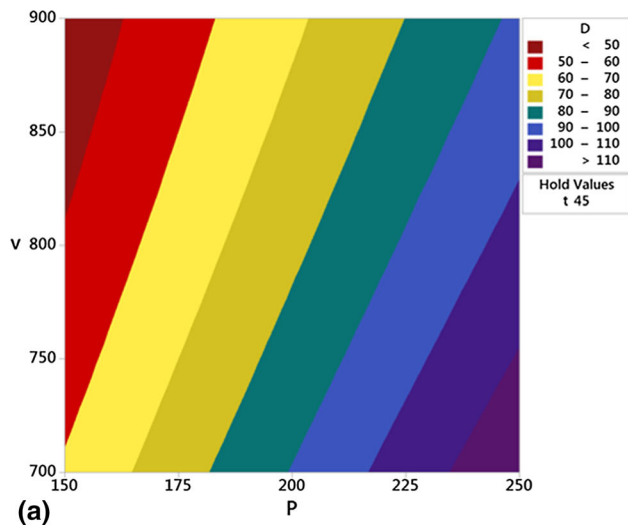


Fig. 13 Contour and surface plot of melt pool depth vs. laser power and scan speed at constant layer thickness

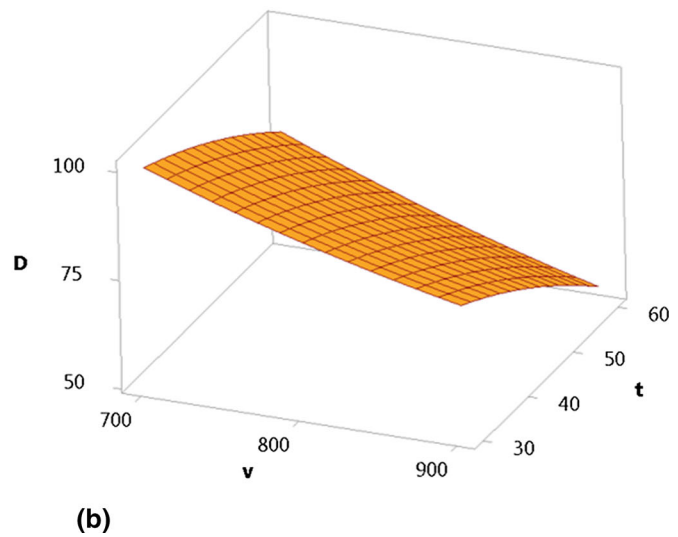
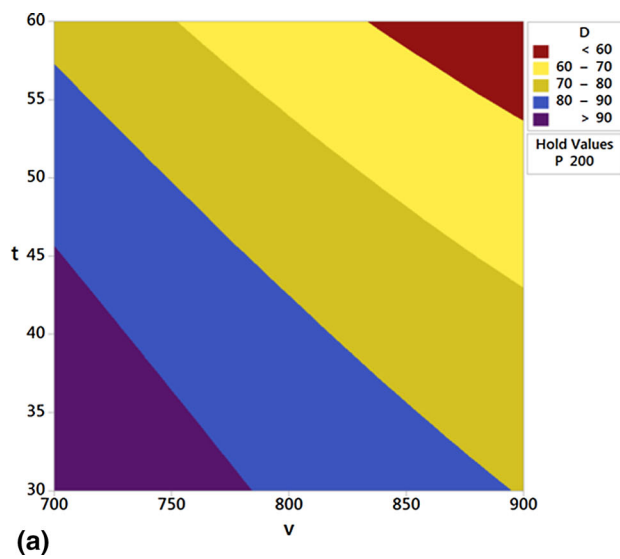


Fig. 14 Contour and surface plot of melt pool depth vs. scan speed and layer thickness at constant laser power

These regression equations were further utilized to predict melt pool depth and width for all process parameter combinations used in BBD design. The predicted values were compared with the actual simulated results. The confirmation test results are shown in Table 11. The maximum percentage error in the prediction of depth and width of melt pool was less than 5 and 2%, respectively.

5.2 Analysis of Variance (ANOVA)

ANOVA tables of responses were developed to analyze the adequacy and significance of regression models. The vital values of linear terms from the ANOVA table are shown in Table 12, and the square terms were omitted due to brevity. The significance of the developed models was examined using the P values (at a 95% confidence level). Model adequacy is

indicated by the obtained P values for the model responses being less than 0.05. T values from coded coefficients represent the quantitative effect of each individual process parameter on response. A positive value reflects the same trend of the concerned factor and response, while negative values show the opposite effect of the factor on the response. Also, the R^2 values were close to 1, which shows a high adequacy of the statistical model.

The residual plots for melt pool depth and width were also developed as shown in Fig. 12 in order to illustrate the model's adequacy. The residuals in the normal probability plot were confirmed to be quite close to the straight line, demonstrating the regression models' good fit. Further, the residual vs. fitted value plot shows that the residuals were randomly distributed and without any particular distribution pattern, indicating good model adequacy.

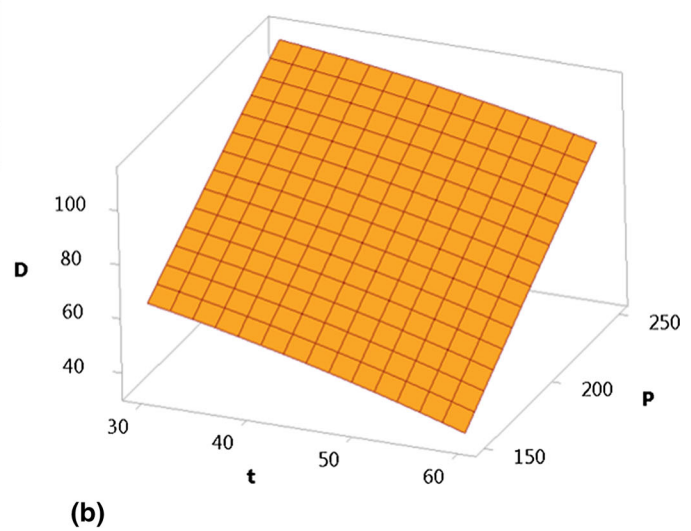
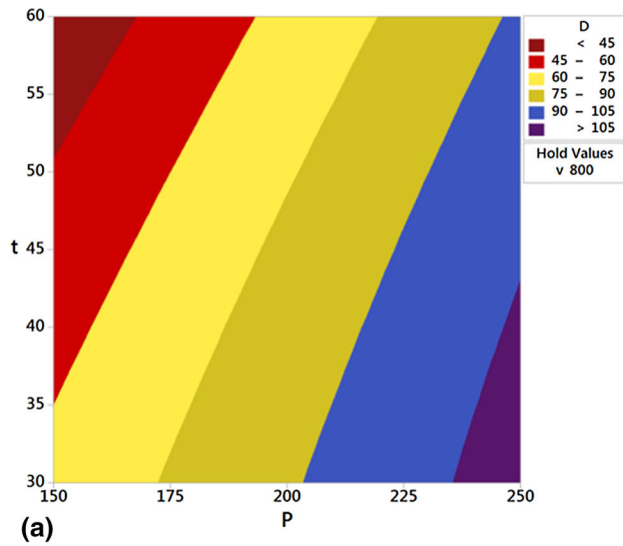


Fig. 15 Contour and surface plot of melt pool depth vs. laser power and layer thickness at constant scan speed

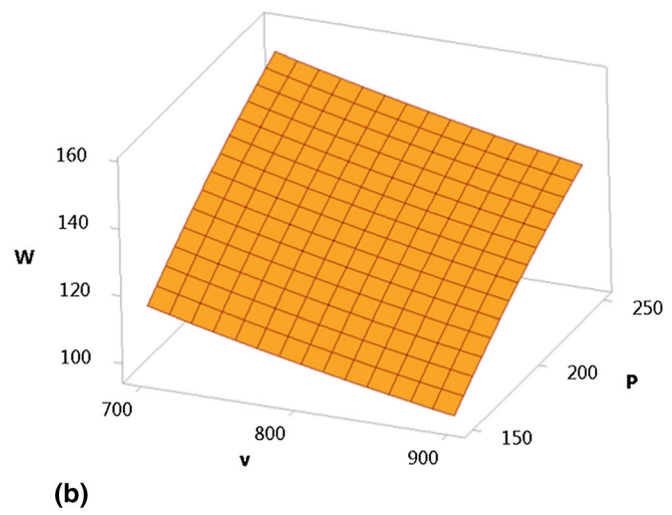
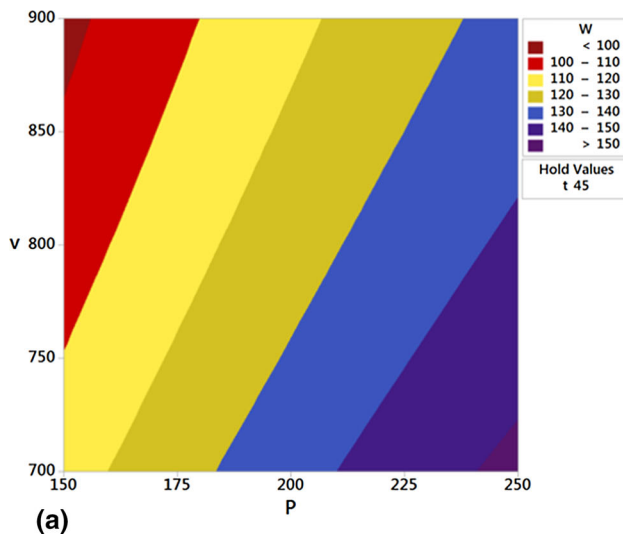


Fig. 16 Contour and surface plot of melt pool width vs. laser power and scan speed at constant layer thickness

5.3 Effects of SLM Process Parameters on the Melt Pool Geometry

To study the variation of the melt pool depth with process parameters (laser power— P , scan speed— v , and layer thickness— t), contour and surface plots were developed as shown in Fig. 13, 14, 15. From contour plots, it is evident that to get a high melt pool depth, higher laser power, lower scan speed, and lower layer thickness are needed. The maximum melt pool depth is obtained on account of increased heat input to the bead. The surface plots clearly show that, for a given layer thickness, the melt pool depth tends to increase as laser power increases and scan speed decreases. At constant scan speed, the lower layer thickness and higher laser power increase the melt pool depth. At constant laser power, lower layer thickness and scan speed increase the melt pool depth. The parametric contribution of laser power, scan speed, and layer thickness to

the melt pool depth was calculated from ANOVA Table 12 as 71.75, 12.76, and 15.47%, respectively.

A similar trend of melt pool width with these process parameters was observed from contour and surface plots (see Fig. 16, 17, 18). The parametric contribution of laser power, scan speed, and layer thickness to melt pool width was calculated from ANOVA Table 12 as 55.52, 14.65, and 29.82%, respectively.

The main effect plots shown in Fig. 19 were analyzed to evaluate the influence of various levels of input process parameters on melt pool geometry. The main effect plots clearly show that while laser power has a positive correlation with melt pool geometry, scan speed and layer thickness have a negative correlation. The most significant parameter for melt pool geometry is confirmed to be laser power. However, scan speed and layer thickness also affect the melt pool geometry due to changes in heat input to the bead.

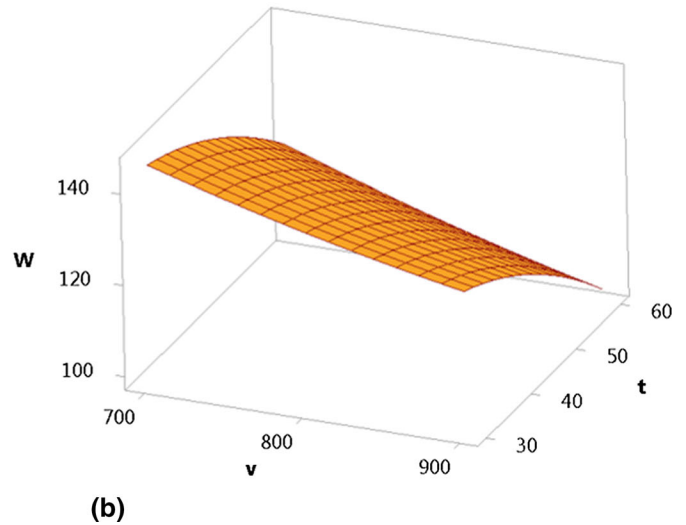
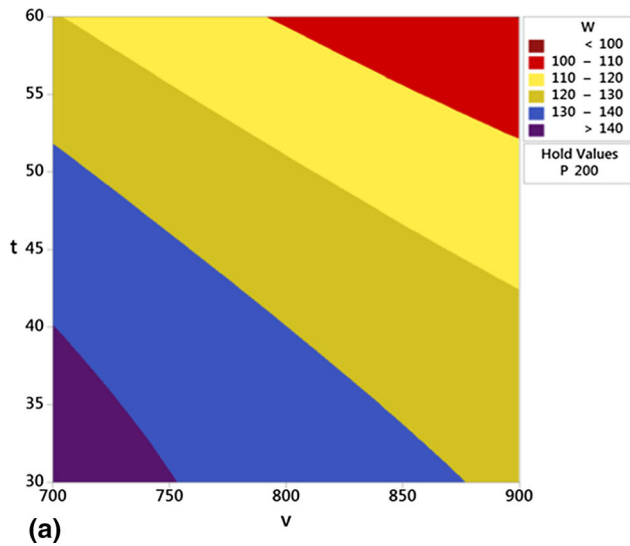


Fig. 17 Contour and surface plot of melt pool width vs. scan speed and layer thickness at constant laser power

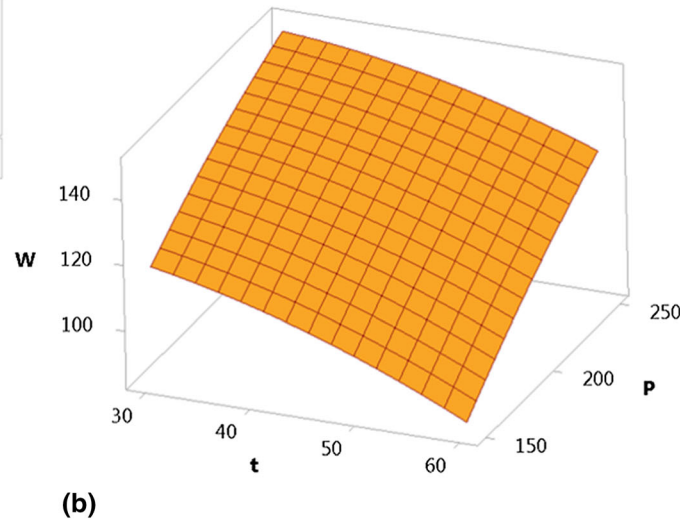
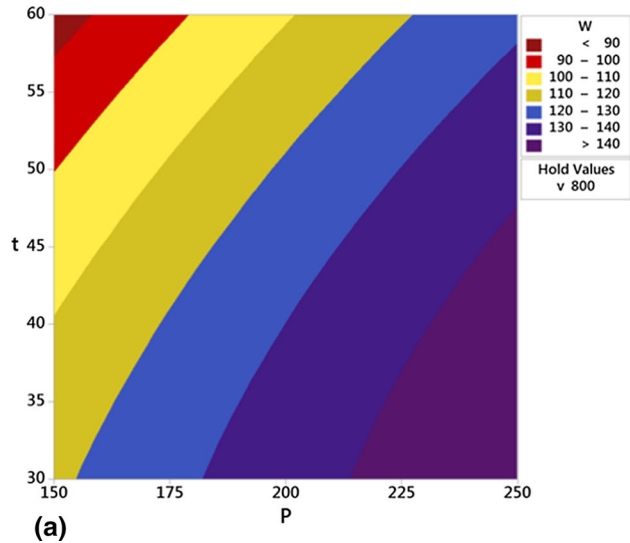


Fig. 18 Contour and surface plot of melt pool width vs. laser power and layer thickness at constant scan speed

The RSM technique was used to optimize the SLM process parameters for defect-free build because controlling the melt pool depth and width can reduce the occurrence of common process-induced defects. Results of optimization are shown in Fig. 20. The optimized process parameters are 240 W laser power, 900 mm/s scan speed, and 45 μm layer thickness to obtain a melt pool geometry with a depth of 95 μm and a width of 130 μm to avoid process-induced defects with a faster build rate. Similarly, one can tailor the melt pool characteristics by choosing process parameters with the help of process maps and regression modeling without encountering common defects in SLM build. By tailoring scan speed and layer thickness within

the safe processing window, the build rate can also be optimized for greater yield.

6. Conclusions

In this work, a numerical modeling approach was employed for the simulation of the melt pool geometry of single-track SLMed Inconel 718. Model validations exhibited that the simulated melt pool geometries were in very good agreement with the actual results reported in the literature. Nine single

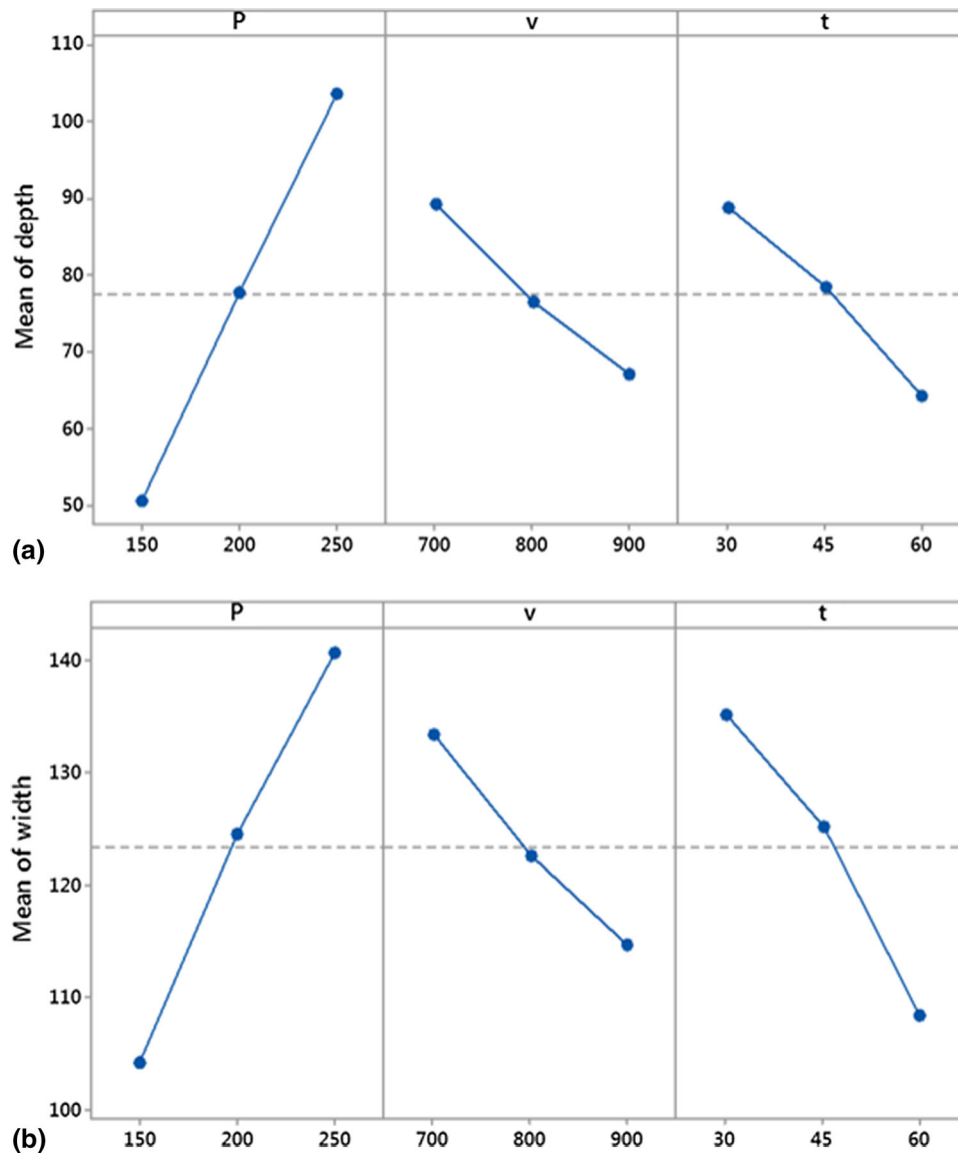


Fig. 19 Main effect plots for (a) mean MP depth (b) mean MP width as a function of P , v and t

tracks were simulated using single bead simulation utilizing different combinations of laser power and scan speed, yielding varying energy density and generating melt pool depths and widths. It was concluded that with an increase in laser power and decrease in scan speed, the melt pool depth and width increase due to more energy being transferred to the powder bed. The simulated melt pool geometry, corresponding to varying laser power and scan speed, was further utilized in the generation of the process map for SLMed Inconel 718, which can be used to avoid common process-induced defects such as lack of fusion, keyholing, and balling during SLM build. Box–Behnken design of response surface methodology was used to study the effect of laser power, scan speed, and layer thickness on the melt pool geometry. Laser power is found to be the most significant SLM process parameter for melt pool geometry. Confirmation test results show that the error in prediction of melt pool geometry with regression modeling is within the acceptable range. SLM

process parameter optimization for defect-free build was also performed using regression modeling. Existing studies show that the optimized parameters can be utilized to print defect-free IN718 builds for better performance. Considering the computation time required in single bead simulations, the proposed numerical approach can be used in the rapid prediction of melt pool geometry in bulk SLM builds and also optimization of process parameters through process maps.

Optimum process parameter settings obtained from the developed process maps can be used to simulate the temperature distribution and microstructure in multi-track multi-layered SLMed builds. This is a work in progress currently. This will further lead to the development of process–structure (P–S) and process–structure–property (P–S–P) linkage for the SLM. ML-based predictive models can also be developed using the simulated data to further automate the evaluation of the melt pool geometry for a given input of process parameters.

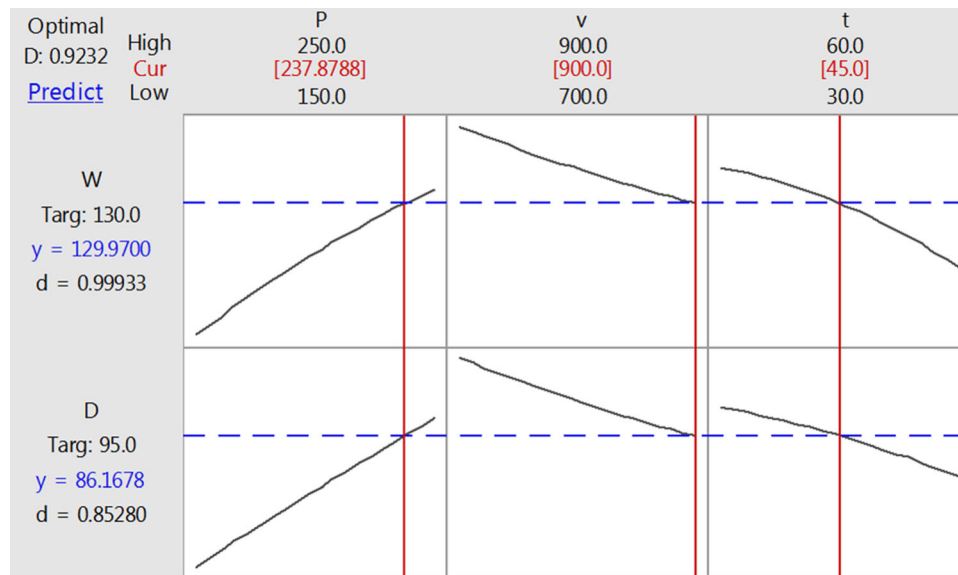


Fig. 20 Optimum process parameters to minimize the defects by tailoring melt pool geometry

Acknowledgments

The Ministry of Human Resource Development, Government of India, is sincerely acknowledged by the lead author for providing financial assistance in the form of a research scholarship. This research received no particular funding in any form.

Conflict of interest

The authors declare that there is no conflict of interest.

References

1. W.E. Frazier, Metal Additive Manufacturing: A Review, *J. Mater. Eng. Perform.*, 2014, **23**, p 1917–1928.
2. D.G. Ahn, Direct Metal Additive Manufacturing Processes and their Sustainable Applications for Green Technology: A Review, *Int. J. Precis. Eng. Manuf. Green. Technol.*, 2016, **3**, p 381–395.
3. M. Seifi, M. Gorelik, J. Waller, N. Hrabe, N. Shamsaei, S. Daniewicz and J.J. Lewandowski, Progress Towards Metal Additive Manufacturing Standardization to Support Qualification and Certification, *JOM*, 2017, **69**(3), p 439–455.
4. P. Kumar, J. Farah, J. Akram, C. Teng, J. Ginn and M. Misra, Influence of Laser Processing Parameters on Porosity in INCONEL 718 During Additive Manufacturing, *Int. J. Adv. Manuf. Technol.*, 2019, **103**, p 1497–1507.
5. N. Kladovasilakis, P. Charalampous, I. Kostavelis, D. Tzetzis and D. Tzouvaras, Impact of Metal Additive Manufacturing Parameters on the Powder Bed Fusion and Direct Energy Deposition Processes: A Comprehensive Review, *Prog. Addit. Manuf.*, 2021, **6**, p 349–365.
6. M.A. Ryder, C.J. Montgomery, M.J. Brand, J.S. Carpenter, P.E. Jones, A.G. Spangenberg and D.A. Lados, Melt Pool and Heat Treatment Optimization for the Fabrication of High-Strength and High-Toughness Additively Manufactured 4340 Steel, *J. Mater. Eng. Perform.*, 2021, **30**, p 5426–5440.
7. H. Ali, H. Ghadbeigi and K. Mumtaz, Processing Parameter Effects on Residual Stress and Mechanical Properties of Selective Laser Melted Ti6Al4V, *J. Mater. Eng. Perform.*, 2018, **27**, p 4059–4068.
8. W.E. King, H.D. Barth, V.M. Castillo, G.F. Gallegos, J.W. Gibbs, J.W. Gibbs, D.E. Hahn, C. Kamath and A.M. Rubenchik, Observation of Keyhole-mode Laser Melting in Laser Powder-bed Fusion Additive Manufacturing, *J. Mater. Process. Technol.*, 2014, **214**, p 2915–2925.
9. T. DebRoy, H.L. Wei, J.S. Zuback, T. Mukherjee, J.W. Elmer, J.O. Milewski, A.M. Beese, A.E. Wilson-Heid, A. De and W. Zhang, Additive Manufacturing of Metallic Components- PROCESS, Structure and Properties, *Prog. Mater. Sci.*, 2018, **92**, p 112–224.
10. P. Promopattum and S.C. Yao, Analytical Evaluation of Defect Generation for Selective Laser Melting of Metals, *Int. J. Adv. Manuf. Technol.*, 2019, **103**, p 1185–1198.
11. W.R. Kim, G.B. Bang, J.H. Park, T.W. Lee, B.S. Lee, S.M. Yang, G.H. Kim, K. Lee and H.G. Kim, Microstructural Study on a Fe-10Cu Alloy Fabricated by Selective Laser Melting for Defect-Free Process Optimization Based on the Energy Density, *J. Mater. Res. Technol.*, 2020, **9**(6), p 12834–12839.
12. S. Gao, X. Yan, C. Chang, E. Aubry, M. Liu, H. Liao and N. Fenineche, Effect of Laser Energy Density on Surface Morphology, Microstructure, and Magnetic Properties of Selective Laser Melted Fe-3wt.% Si Alloys, *J. Mater. Eng. Perform.*, 2021, **30**, p 5020–5030.
13. J.J.S. Dilip, S. Zhang, C. Teng, K. Zeng, C. Robinson, D. Pal and B.E. Stucker, Influence of Processing Parameters on the Evolution of Melt Pool, Porosity, and Microstructures in Ti-6Al-4V Alloy Parts Fabricated by Selective Laser Melting, *Prog. Addit. Manuf.*, 2017, **2**, p 157–167.
14. X. Zhang, B. Mao, L. Mushongera, J. Kundin and Y. Liao, Laser Powder Bed Fusion of Titanium Aluminides: An Investigation on Site-Specific Microstructure Evolution Mechanism, *Mater. Des.*, 2021, **201**, 109501.
15. T.G. Spears and S.A. Gold, In-process Sensing in Selective Laser Melting (SLM) Additive Manufacturing, *Integr. Mater. Manuf. Innov.*, 2016, **5**, p 16–40.
16. S. Shrestha and K. Chou, Single Track Scanning Experiment in Laser Powder Bed Fusion Process, *Proced. Manuf.*, 2018, **26**, p 857–864.
17. L. Scime and J.L. Beuth, Melt Pool Geometry and Morphology Variability for the Inconel 718 Alloy in a Laser Powder Bed Fusion Additive Manufacturing Process, *Addit. Manuf.*, 2019, **29**, 100830.
18. S.A. Khairallah and A.T. Anderson, Mesoscopic Simulation Model of Selective Laser Melting of Stainless-Steel Powder, *J. Mater. Process. Technol.*, 2014, **214**, p 2627–2636.
19. B. Cheng, L. Loeber, H. Willeck, U. Hartel and C. Tuffile, Computational Investigation of Melt Pool Process Dynamics and Pore Formation in Laser Powder Bed Fusion, *J. Mater. Eng. Perform.*, 2019, **28**, p 6565–6578.
20. M. Khorasani, A.H. Ghasemi, M. Leary, L. Cordova, E. Sharabian, E. Farabi, I. Gibson, M. Brandt and B. Rolfe, A Comprehensive Study on Meltpool Depth in Laser-based Powder Bed Fusion of Inconel 718, *Int. J. Adv. Manuf. Technol.*, 2022, **120**, p 2345–2362.
21. S.A. Khairallah, A.T. Anderson, A.M. Rubenchik and W.E. King, Laser Powder-bed Fusion Additive Manufacturing: Physics of Complex Melt Flow and Formation Mechanisms of Pores, Spatter, and Denudation Zones, *Acta Mater.*, 2016, **108**, p 36–45.

22. N. Diaz Vallejo, C. Lucas, N. Ayers, K. Graydon, H. Hyer and Y. Sohn, Process Optimization and Microstructure Analysis to Understand Laser Powder Bed Fusion of 316L Stainless Steel, *Metals*, 2021, **11**, p 832.
23. S. Jelvani, R. Shoja Razavi, M. Barekat and M. Dehnavi, Empirical-Statistical Modeling and Prediction of Geometric Characteristics for Laser-Aided Direct Metal Deposition of Inconel 718 Superalloy, *Met. Mater. Int.*, 2019, **26**, p 668–681.
24. M. Balichakra, S. Bontha, P. Krishna and V.K. Balla, Laser Surface Melting of γ -TiAl Alloy: An Experimental and Numerical Modelling Study, *Mater. Res. Expr.*, 2019, **6**, 046543.
25. P. Tan, F. Shen, B. Li and K. Zhou, A Thermo-metallurgical-Mechanical Model for Selective Laser Melting of Ti6Al4V, *Mater. Des.*, 2019, **168**, 107642.
26. Y.M. Arisoy, L.E. Criales and T.R. Ozel, Modelling and Simulation of Thermal Field and Solidification in Laser Powder Bed Fusion of Nickel Alloy IN625, *Opt. Laser Technol.*, 2019, **109**, p 278–292.
27. M.J. Ansari, D.S. Nguyen and H.S. Park, Investigation of SLM Process in Terms of Temperature Distribution and Melting Pool Size: Modeling and Experimental Approaches, *Materials*, 2019, **12**, p 1272.
28. S. Waqar, Q. Sun, J. Liu, K. Guo and J. Sun, Numerical Investigation of Thermal Behavior and Melt Pool Morphology in Multi-track Multi-layer Selective Laser Melting of the 316L Steel, *Int. J. Adv. Manuf. Technol.*, 2021, **112**, p 879–895.
29. M. Majeed, H.M. Khan, G. Wheatley and R. Situ, A Numerical Approach to Assess the Impact of the SLM Laser Parameters on Thermal Variables, *J. Addit. Manuf. Technol.*, 2021, **1**(3), p 589–589.
30. C. Wang, X.P. Tan, S.B. Tor and C.S. Lim, Machine Learning in Additive Manufacturing: State-of-the-Art and Perspectives, *Addit. Manuf.*, 2020, **36**, 101538.
31. N. Kouraytem, X. Li, W. Tan, B. Kappes and A.D. Spear, Modeling Process–Structure–Property Relationships in Metal Additive Manufacturing: A Review on Physics-Driven Versus Data-Driven Approaches, *J. Phys. Mater.*, 2021, **4**, 032002.
32. X. Qi, G. Chen, Y. Li, X. Cheng and C. Li, Applying Neural-Network-Based Machine Learning to Additive Manufacturing: Current Applications Challenges and Future Perspectives, *Engineering*, 2019, **5**, p 721–729.
33. E. Maleki, S. Bagherifard and M. Guagliano, Application of Artificial Intelligence to Optimize the Process Parameters Effects on Tensile Properties of Ti-6Al-4V Fabricated by Laser Powder-Bed Fusion, *Int. J. Mech. Mater. Des.*, 2022, **18**, p 199–222.
34. H. Tupac-Yupanqui and A. Armani, Additive Manufacturing of Functional Inconel 718 Parts from Recycled Materials, *J. Mater. Eng. Perform.*, 2021, **30**, p 1177–1187.
35. Y. Li and D. Gu, Parametric Analysis of Thermal Behaviour During Selective Laser Melting Additive Manufacturing of Aluminium Alloy Powder, *Mater. Des.*, 2014, **63**, p 856–867.
36. J. Yin, H. Zhu, L. Ke, W. Lei, C. Dai and D. Zuo, Simulation of Temperature Distribution in Single Metallic Powder Layer for Laser Micro-Sintering, *Comput. Mater. Sci.*, 2012, **53**, p 333–339.
37. P. He, C. Sun and Y. Wang, Material Distortion in Laser-Based Additive Manufacturing of Fuel Cell Component: Three-Dimensional Numerical Analysis, *Addit. Manuf.*, 2021, **46**, 102188.
38. J.P. Choi, G.H. Shin, S. Yang, D.Y. Yang, J.S. Lee, M. Brochu and J.H. Yu, Densification and Microstructural Investigation of Inconel 718 Parts Fabricated by Selective Laser Melting, *Powder Technol.*, 2017, **310**, p 60–66.
39. W.Y. Chen, X. Zhang, M. Li, R. Xu, C. Zhao and T. Sun, Laser Powder Bed Fusion of INCONEL 718 on 316 Stainless Steel, *Addit. Manuf.*, 2020, **36**, 101500.
40. T.E. Shelton, G.R. Cobb, C.R. Hartsfield, B.M. Doane, C.C. Eckley and R.A. Kemnitz, The Impact of Laser Control on the Porosity and Microstructure of Selective Laser Melted Nickel Superalloy 718, *Results Mater.*, 2021, **11**, 100211.
41. O. Gokcekaya, T. Ishimoto, S. Hibino, J. Yasutomi, T. Narushima and T. Nakano, Unique Crystallographic Texture Formation in Inconel 718 by Laser Powder Bed Fusion and Its Effect on Mechanical Anisotropy, *Acta Mater.*, 2021, **212**, 116876.
42. M. Bayat, S. Mohanty and J.H. Hattel, Multiphysics Modelling of Lack-of-Fusion Voids Formation and Evolution in IN718 Made by Multi-Track/multi-Layer L-PBF, *Int. J. Heat Mass. Transf.*, 2019, **139**, p 95–114.
43. C. Kusuma, S.H. Ahmed, A. Mian and R. Srinivasan, Effect of Laser Power and Scan Speed on Melt Pool Characteristics of Commercially Pure Titanium, *J. Mater. Eng. Perform.*, 2017, **26**, p 3560–3568.
44. J. Jakumeit, C. Huang, R. Laqua, J. Zielinski and J.H. Schleifenbaum, Effect of Evaporated Gas Flow on Porosity and Microstructure of IN718 Parts Produced by LPBF-Processes, *IOP Conf. Ser. Mater. Sci. Eng.*, 2020, **861**, p 012011.
45. U. Segurajauregi, A. Alvarez-Vazquez, M. Muniz-Calvente, I. Urresti and H. Naveiras, Fatigue Assessment of Selective Laser Melted Ti-6Al-4V: Influence of Speed Manufacturing and Porosity, *Metals*, 2021, **11**, p 1022.
46. P. Kumar, P. Chakravarthy, S.K. Manwatkar and S. Murty, Effect of Scan Speed and Laser Power on the Nature of Defects, Microstructures and Microhardness of 3D-Printed Inconel 718 Alloy, *J. Mater. Eng. Perform.*, 2019, **28**, p 6565–6578.

Publisher's Note Springer Nature remains neutral with regard to jurisdictional claims in published maps and institutional affiliations.

Springer Nature or its licensor (e.g. a society or other partner) holds exclusive rights to this article under a publishing agreement with the author(s) or other rightsholder(s); author self-archiving of the accepted manuscript version of this article is solely governed by the terms of such publishing agreement and applicable law.